World Academy of Science, Engineering and Technology
International Journal of Physical and Mathematical Sciences
Vol:16, No:11, 2022

An Axisymmetric Finite Element Method for Compressible Swirling Flow

Raphael Zanella, Todd A. Oliver, Karl W. Schulz

Abstract—This work deals with the finite element approximation of axisymmetric compressible flows with swirl velocity. We are interested in problems where the flow, while weakly dependent on the azimuthal coordinate, may have a strong azimuthal velocity component. We describe the approximation of the compressible Navier-Stokes equations with H^1-conformal spaces of axisymmetric functions. The weak formulation is implemented in a C++ solver with explicit time marching. The code is first verified with a convergence test on a manufactured solution. The verification is completed by comparing the numerical and analytical solutions in a Poiseuille flow case and a Taylor-Couette flow case. The code is finally applied to the problem of a swirling subsonic air flow in a plasma torch geometry.

Keywords—Axisymmetric problem, compressible Navier-Stokes equations, continuous finite elements, swirling flow.

I. Introduction

We present a finite element method for the compressible Navier-Stokes equations with assumed axisymmetry. The target application is an inductively coupled plasma (ICP) torch, or simply "plasma torch" in this article. An ICP torch is a tube-like system where the injected gas (e.g. air or argon) is subjected to an alternating magnetic field generated by an induction coil. Assuming the feed gas has become partially ionized, the electric field generated by the alternating magnetic field accelerates the electrons, which subsequently heat the gas. The performance of such a device can be sensitive to the fluid flow, which is the subject of investigation here. The geometry of the torch is roughly symmetric with respect to the centerline of the tube. An axisymmetric model allows to gain insights about the torch physics [1], [2] and is much more efficient in terms of computational time than a 3D model. We are particularly interested in a device used for material testing at high temperature [3]. The azimuthal velocity needs to be accounted for because the gas is injected tangentially to create a strong swirling flow inside the tube. We therefore do not neglect this component in our method as it is sometimes done in the literature. A finite volume method solving the axisymmetric compressible Euler equations, with this specific application in mind, was presented in [4]. In this work, we consider the viscous terms of the equations and use the finite element method. The weak formulation is established with a similar approach as the work [5] on the axisymmetric compressible Euler equations.

R. Zanella, T. A. Oliver and K. W. Schulz are with the Oden Institute for Computational Engineering and Sciences, University of Texas, Austin, TX 78712 USA (e-mail: zanella@oden.utexas.edu, oliver@oden.utexas.edu, karl@oden.utexas.edu)

After this first introductory section, the article is organized as follows. The second section details the equations of the problem. The third section describes the numerical method, in particular the derivation of the axisymmetric weak formulation and the time integration method. The fourth, fifth and sixth sections present the different test cases used to verify the implementation. The last section is dedicated to the simulation of a subsonic air flow in an experimental plasma torch, which illustrates the utility of the method.

II. Governing Equations

The conservation equations of mass, momentum and energy write

$$\frac{\partial \rho}{\partial t} + \nabla\cdot(\rho\mathbf{u}) = 0, \tag{1}$$

$$\frac{\partial \rho\mathbf{u}}{\partial t} + \nabla\cdot(\rho\mathbf{u}\otimes\mathbf{u}) = \nabla\cdot[\sigma] + \rho\mathbf{g}, \tag{2}$$

$$\frac{\partial \rho E}{\partial t} + \nabla\cdot\left(\rho E\mathbf{u}\right) = \nabla\cdot([\sigma]\cdot\mathbf{u}) + \rho\mathbf{g}\cdot\mathbf{u} - \nabla\cdot\mathbf{q}, \tag{3}$$

where ρ is the mass density, $\mathbf{u}$ is the velocity, p is the pressure, $[\sigma]$ is the stress tensor, $\mathbf{g} = -g\mathbf{e}_z$ is the acceleration due to gravity, E is the total energy per unit mass and $\mathbf{q}$ is the heat flux vector. The stress tensor is written as $[\sigma] = -p[1] + [\tau]$, where p is the pressure and $[\tau]$ is the viscous stress tensor. The total energy per unit mass is given by $E = e + \frac{u^2}{2}$, where e is the internal energy per unit mass.

We denote by T the temperature and by $h = e + \frac{p}{\rho}$ the enthalpy per unit mass. The gas is assumed ideal so that we have

$$p = \rho R T, \tag{4}$$

where R is the specific gas constant. We also have

$$e = c_v T \qquad \text{and} \qquad h = c_p T, \tag{5}$$

where c_v is the specific heat at constant volume and c_p is the specific heat at constant pressure. We denote by $\gamma = c_p/c_v$ the ratio of the specific heats. The specific heats can be expressed as a function of R and γ:

$$c_v = \frac{R}{\gamma - 1} \qquad \text{and} \qquad c_p = \frac{\gamma R}{\gamma - 1}. \tag{6}$$

The viscous stress tensor is given by a Newtonian law

$$[\tau] = 2\eta\left(\frac{1}{2}\left(\nabla\mathbf{u} + (\nabla\mathbf{u})^T\right) - \frac{1}{3}\nabla\cdot\mathbf{u}[I]\right), \tag{7}$$

where η is the dynamic viscosity. The dynamic viscosity is temperature dependent through a power law

$$\eta = \eta_{ref}\left(\frac{T}{T_{ref}}\right)^{n_{pl}}, \tag{8}$$

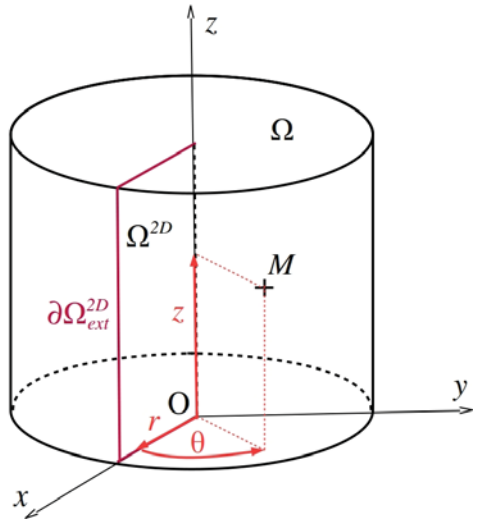

Fig. 1 Example of cylindrical domain of computation Ω and the associated meridian section Ω^{2D}. A point $M \in \Omega$ is located by its cylindrical coordinates (r, θ, z), with $(r, z) \in \Omega^{2D}$ and $\theta \in [0, 2\pi)$

where η_{ref}, T_{ref} and n_{pl} are constants. The heat flux vector is given by a Fourier law

$$\mathbf{q} = -\lambda \nabla T, \tag{9}$$

where λ is the thermal conductivity. The thermal conductivity is given by

$$\lambda = \frac{\eta c_p}{P_r}, \tag{10}$$

where P_r is the Prandtl number, assumed constant.

We use the cylindrical coordinates (r, θ, z). We denote by u_r, u_θ and u_z the radial, azimuthal and axial velocity components, respectively. We do not expand the equations in cylindrical coordinates for the sake of brevity. The equations under the axisymmetry assumption are obtained by applying $\frac{\partial}{\partial \theta} = 0$ to the equations in cylindrical coordinates.

III. Numerical Method

We first present the space approximation of the problem and then the time integration method, along with details on the implementation.

A. Axisymmetric Weak Formulation

We denote by Ω the axisymmetric computational domain and by $\partial\Omega$ its boundary. We denote by Ω^{2D} the half meridian section, say at $\theta = 0$, of Ω and by $\partial\Omega^{2D}$ its boundary. We note $\partial\Omega^{2D}_{ext} = \partial\Omega^{2D} \cap \partial\Omega$. An illustration is presented in Fig. 1.

Let $\mathcal{T}_h$ be a mesh of Ω^{2D} with characteristic mesh size h. We denote by K a cell of $\mathcal{T}_h$. Let $p \in \mathbb{N}^*$ be the order of the polynomial approximation. We define the approximation space for scalar functions

$$V = \left\{ v \in \mathcal{C}^0\left(\overline{\Omega}; \mathbb{R}\right);\ \exists v^{2D} \in V^{2D};\ v(r,\theta,z) = v^{2D}(r,z),\ \forall (r,\theta,z) \right\}, \tag{11}$$

where

$$V^{2D} = \left\{ v \in \mathcal{C}^0\left(\overline{\Omega^{2D}}; \mathbb{R}\right);\ v_{|_K} \in \mathbb{P}_p,\ \forall K \in \mathcal{T}_h \right\}. \tag{12}$$

We also define the approximation space for vector functions $\mathbf{V} = V^3$. While ρ and ρE reside in V, $\rho\mathbf{u}$ resides in $\mathbf{V}$. We introduce the test spaces $V_{0,\rho}$, $\mathbf{V}_0$ and $V_{0,\rho E}$ for ρ, $\rho\mathbf{u}$ and ρE respectively, which are appropriately defined taking into account the Dirichlet boundaries. This section is independent of the boundary conditions considered. The boundary conditions are detailed for each treated case in the following sections. Note that the axisymmetry assumption always imposes to enforce $u_r = u_\theta = 0$ at $r = 0$.

An important result used in the following is that, for every axisymmetric function f defined in $\overline{\Omega}$, we can write

$$\int_\Omega f dV = 2\pi \int_{\Omega^{2D}} f r dS \tag{13}$$

and

$$\int_{\partial\Omega} f dS = 2\pi \int_{\partial\Omega^{2D}_{ext}} f r dL, \tag{14}$$

where dV, dS and dL designate an elementary volume, an elementary surface and an elementary length, respectively. This means that an integral over Ω of an axisymmetric integrand can be reduced to an integral over Ω^{2D} (and analogous result for an integral over $\partial\Omega$).

The weak formulation is obtained by multiplying by test functions (1)-(3) and by then integrating over Ω. Because the trial and test functions are axisymmetric, we can apply (13) and (14) to the result. We denote by $t_f > 0$ the final time. The weak formulation is expressed: find $\rho \in \mathcal{C}^1([0,t_f]; V)$, $\rho\mathbf{u} \in \mathcal{C}^1([0,t_f]; \mathbf{V})$ and $\rho E \in \mathcal{C}^1([0,t_f]; V)$ satisfying the boundary conditions such that

$$\begin{aligned} \int_{\Omega^{2D}} \frac{d\rho}{dt} v r dS = &\int_{\Omega^{2D}} \rho\mathbf{u} \cdot \nabla v r dS \\ &- \int_{\partial\Omega^{2D}_{ext}} v \rho\mathbf{u} \cdot \mathbf{n} r dL,\ \forall v \in V_{0,\rho}; \end{aligned} \tag{15}$$

$$\begin{aligned} \int_{\Omega^{2D}} \frac{d\rho\mathbf{u}}{dt} \cdot \mathbf{v} r dS = &\int_{\Omega^{2D}} (\rho\mathbf{u} \otimes \mathbf{u}) : \nabla\mathbf{v} r dS \\ &- \int_{\partial\Omega^{2D}_{ext}} ((\rho\mathbf{u} \otimes \mathbf{u}) \cdot \mathbf{v}) \cdot \mathbf{n} r dL \\ &- \int_{\Omega^{2D}} [\sigma] : \nabla\mathbf{v} r dS \\ &+ \int_{\partial\Omega^{2D}_{ext}} ([\sigma] \cdot \mathbf{v}) \cdot \mathbf{n} r dL \\ &+ \int_{\Omega^{2D}} \rho\mathbf{g} \cdot \mathbf{v} r dS,\ \forall \mathbf{v} \in \mathbf{V}_0; \end{aligned} \tag{16}$$

$$\begin{aligned} \int_{\Omega^{2D}} \frac{d\rho E}{dt} v r dS = &\int_{\Omega^{2D}} \rho E\mathbf{u} \cdot \nabla v r dS \\ &- \int_{\partial\Omega^{2D}_{ext}} v \rho E\mathbf{u} \cdot \mathbf{n} r dL \\ &- \int_{\Omega^{2D}} ([\sigma] \cdot \mathbf{u} - \mathbf{q}) \cdot \nabla v r dS \\ &+ \int_{\partial\Omega^{2D}_{ext}} v([\sigma] \cdot \mathbf{u} - \mathbf{q}) \cdot \mathbf{n} r dL \\ &+ \int_{\Omega^{2D}} \rho\mathbf{u} \cdot \mathbf{g} v r dS,\ \forall v \in V_{0,\rho E}. \end{aligned} \tag{17}$$

The boundary terms may vanish due to either the quantities enforced or the fact that the test function is zero at the boundary (Dirichlet boundary). Because the trial and test functions only depend on the (r, z) coordinates, this weak formulation can be implemented as that of a 2D problem. Note the presence of the r factor in every term. Note also that the gradient of a scalar or vector function in cylindrical coordinates has a different formula compared to in Cartesian coordinates.

B. Time Integration

Let n_{dof} be the number of degrees of freedom per variable and $\mathcal{U} \in \mathcal{C}^1([0, t_f]; \mathbb{R}^{5n_{dof}})$ be the time-dependent vector containing the degrees of freedom of all variables. The weak formulation (15)-(17) can be put under the form of a vector ODE:

$$\begin{cases} \mathcal{M}\dfrac{d\mathcal{U}}{dt}(t) = \mathcal{R}(\mathcal{U}(t)),\ \forall t \in [0, t_f], \\ \mathcal{U}(0) = \mathcal{U}^0, \end{cases} \tag{18}$$

where $\mathcal{M} \in \mathbb{R}^{5n_{dof} \times 5n_{dof}}$ is the mass matrix, $\mathcal{R}$ is a nonlinear function of the degrees of freedom which describes the flux terms and the gravity terms and $\mathcal{U}^0 \in \mathbb{R}^{5n_{dof}}$ contains the degrees of freedom of the initial condition projected in V^5. Note that the r factor in every term of (15)-(17) needs to be taken into account in the mass matrix and the right-hand side definitions. Note also that the mass matrix and the right-hand side are modified to take into account the Dirichlet conditions.

An explicit method is used to solve the system (18). Runge-Kutta methods of different orders are used. The algorithm is implemented in a C++ code based on the MFEM library for finite elements [6].

IV. Test on a Manufactured Solution

The solver is verified with a convergence test on a manufactured solution. The computational domain is a cylinder

$$\Omega = \{(r, \theta, z) \in \mathbb{R}^3;\ 0 \leq r < 0.5,\ 0 \leq \theta < 2\pi,\ 0 < z < 1\}. \tag{19}$$

The manufactured solution is defined by

$$\begin{cases} \rho(r,z,t) = 1 + 50r^2(0.5 - r)^2 \sin(2\pi z)\cos(200\pi t), \\ u_r(r,z,t) = r^2 \sin(2\pi r)\sin(2\pi z)\cos(200\pi t), \\ u_\theta(r,z,t) = r^2 \sin(2\pi r)\sin(2\pi z)\cos(200\pi t), \\ u_z(r,z,t) = r^2(\cos(\pi r)\sin(2\pi z)\cos(200\pi t) - 1) + 0.25, \\ T(r,z,t) = 1 + r^2 \cos(\pi r)\sin(2\pi z)\cos(200\pi t). \end{cases} \tag{20}$$

The lateral surface is treated as an isothermal wall where $\mathbf{u} = \mathbf{0}$ and $T = 1$ is enforced strongly. The top and bottom surfaces are treated as periodic boundaries. An artificial diffusion term is added in (1) because it is necessary to obtain the expected rates at long time. Adequate source terms are implemented in (1)-(3) so that the manufactured solution is solution.

The parameters considered are $R = 0.6$, $\gamma = 1.5$, $\eta_{ref} = 0.1$, $T_{ref} = 2$, $n_{pl} = 0.8$, $\mathrm{Pr} = 0.7$ and $g = 1.5$. We do not specify the units as the parameters do not refer to an actual physical configuration. We are only interested in verifying the code. No units are used in the other test cases (Poiseuille flow and Taylor-Couette flow) for the same reason. We use a rectangular mesh and an order of approximation $p = 1$. The time integration is performed by using a 2^{nd} order Runge-Kutta method.

TABLE I
Manufactured Solution Test

h	$\|U - U_{ex}\|_{L^2(\Omega)}$	COC
0.1	0.013685373	
0.05	0.0035482733	1.947
0.025	0.00089366856	1.989
0.0125	0.00022454565	1.993

Fixed small time step $\tau = 5 \times 10^{-5}$. Errors at final time $t_f = 0.01$

We fix the time step to a very small value so that the error is dominated by the spatial error. We note $U = (\rho, \rho u_r, \rho u_\theta, \rho u_z, \rho E)$. We observe the evolution of the error $\|U - U_{ex}\|_{L^2(\Omega)}$ at final time with the mesh size (the subscript ex designates the exact solution). The results are reported in Tab. I. The computed order of convergence (COC) is $p+1 = 2$ and is therefore consistent with the approximation order.

V. Poiseuille Flow in a Tube

The solver is applied to a gravity-induced Poiseuille flow in a vertical channel. In order to compare the numerical result with an analytical solution, we treat the incompressible case. A source term is implemented in the energy equation so that the final temperature and the final density are uniform.

The computational domain is the cylinder given in (19). The lateral surface is treated as an isothermal wall where $\mathbf{u} = \mathbf{0}$ and $T = T_0$ is enforced strongly. The top and bottom surfaces are treated as periodic boundaries.

The fluid is initially at rest: $\rho = \rho_0$, $\mathbf{u} = \mathbf{0}$ and $T = T_0$ at $t = 0$. We simulate the problem until a steady state is reached. The analytical solution is $\rho = \rho_0$, $T = T_0$ and $\mathbf{u} = u_z(r)\mathbf{e}_z$, with

$$u_z(r) = -\frac{\rho_0 g}{4\eta}(R_0^2 - r^2), \tag{21}$$

where R_0 is the radius of the cylinder.

The parameters considered are $R_0 = 0.5$, $\rho_0 = 1.1$, $T_0 = 1$, $R = 0.6$, $\gamma = 1.5$, $n_{pl} = 0$, $\mathrm{Pr} = 0.7$ and $g = 0.9$. The elements are squares of size $h = 0.025$. The order of approximation is $p = 1$. The time integration is performed by using a 2^{nd} order Runge-Kutta method with a time step $\tau = 2.5 \times 10^{-4}$.

The numerical solution obtained for u_z, at mid-height and at final time is confronted to the analytical solution in Fig. 2 for various $\eta_{ref} = \eta$. The numerical result is very close to the analytical one.

VI. Taylor-Couette Flow

The solver is applied to a Taylor-Couette flow. The flow is driven by the rotation of two concentric walls. Contrary to the Poiseuille flow, this flow has an azimuthal component. Again,

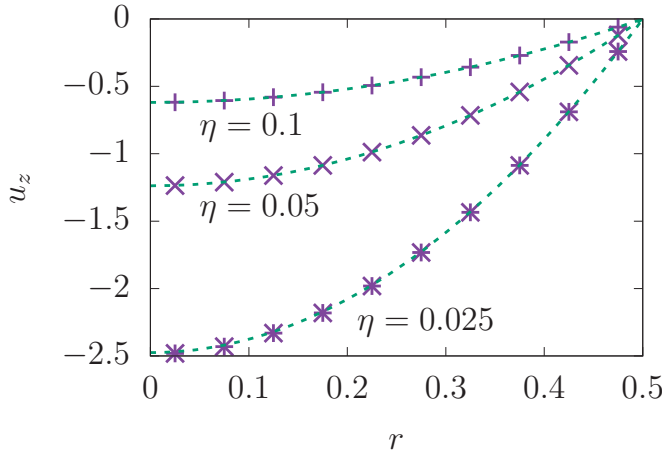

Fig. 2 Poiseuille flow. Numerical (symbols) versus analytical (line) profile of the axial velocity for different viscosities. Mid-height profile $z = 0.5$. Final time $t_f = 10$

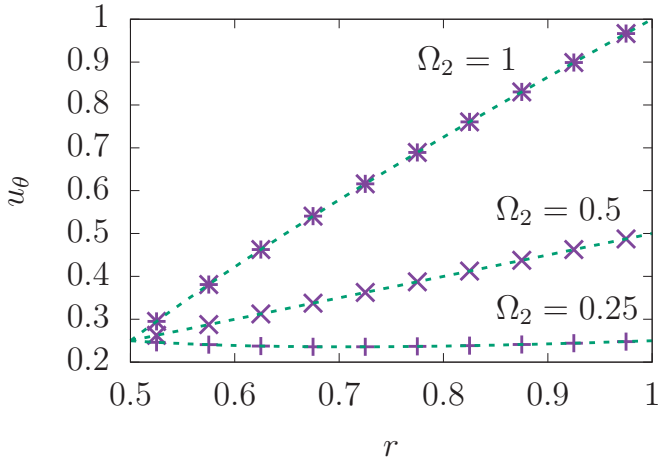

Fig. 3 Taylor-Couette flow. Numerical (symbols) versus analytical (line) profile of the azimuthal velocity for different rotation velocities of the exterior wall. The rotation velocity of the interior wall is $\Omega_1 = 0.5$. Mid-height profile $z = 0.5$. Final time $t_f = 10$

in order to compare the numerical result with an analytical solution, we treat the incompressible case. A source term is implemented in the energy equation so that the final density is uniform.

The computational domain is an annulus

$$\Omega = \{(r, \theta, z) \in \mathbb{R}^3;\ 0.5 < r < 1,\ 0 \leq \theta < 2\pi,\ 0 < z < 1\}. \tag{22}$$

The lateral surfaces are treated as isothermal walls where a velocity and a temperature which are consistent with the initial condition are enforced strongly. The top and bottom surfaces are treated as periodic boundaries.

We denote by R_1 and R_2 the internal and external radii of the annulus, respectively. We denote by Ω_1 and Ω_2 the rotation velocities of the internal and external walls, respectively. We introduce the parameters

$$A = \frac{\Omega_2 R_2^2 - \Omega_1 R_1^2}{R_2^2 - R_1^2} \quad \text{and} \quad B = \frac{(\Omega_1 - \Omega_2) R_1^2 R_2^2}{R_2^2 - R_1^2}. \tag{23}$$

The fluid is initially at rest: $\rho = \rho_0$, $\mathbf{u} = u_\theta(r)\mathbf{e}_\theta$, with

$$u_\theta(r) = \begin{cases} 0 & \text{if } R_1 < r < R_2, \\ Ar + \dfrac{B}{r} & \text{if } r = R_1 \text{ or } R_2, \end{cases} \tag{24}$$

and

$$T = T_0 + \frac{B^2(r^2 - R_1^2) + r^2 R_1^2 \left(A^2(r^2 - R_1^2) + 4AB \log\left(\frac{r}{R_1}\right)\right)}{2r^2 R_1^2 c_v(\gamma - 1)} \tag{25}$$

at $t = 0$. We simulate the problem until a steady state is reached. The analytical solution is $\rho = \rho_0$, T given by (25) and $\mathbf{u} = u_\theta(r)\mathbf{e}_\theta$, with

$$u_\theta(r) = Ar + \frac{B}{r}. \tag{26}$$

The parameters considered are $R_1 = 0.5$, $R_2 = 1$, $\rho_0 = 1.1$, $T_0 = 1$, $R = 0.6$, $\gamma = 1.5$, $\eta_{ref} = \eta = 0.1$, $n_{pl} = 0$ and $g = 0$. The elements are squares of size $h = 0.025$. The order of approximation is $p = 1$. The time integration is performed by using a 2^{nd} order Runge-Kutta method with a time step $\tau = 2.5 \times 10^{-4}$.

The numerical solution obtained for u_θ, at mid-height and at final time is confronted to the analytical solution in Fig. 3 for various Ω_2 while Ω_1 is fixed. Again, the numerical result is very close to the analytical one.

VII. Swirling Flow in a Plasma Torch

We simulate an air flow in an experimental plasma torch geometry close to [3]. The torch is a tube-like system with a length of approximately 35 cm and a maximum diameter of approximately 5.6 cm. The air is injected laterally from the bottom by 4 channels of small and square section equally spaced. The air is introduced with a non-zero angle with respect to the normal of the lateral wall, which produces the swirl. The air escapes the system through a nozzle at the top. Schematics with accurate dimensions are presented in Figs. 4-6. The injected mass flow is 40 slpm, considering a standard air density at 25°C.

The main challenge is the axisymmetric modeling of the system considering that the inlets are not arranged in an axisymmetric manner. We model the inlets by an axisymmetric inlet, i.e. an inlet that goes all around the bottom of the torch, whose height is approximately the same as that of the actual inlets.

We denote by p_0 and T_0 the ambient pressure and temperature. The wall is treated as an isothermal wall where $T = T_0$ and $\mathbf{u} = \mathbf{0}$ is enforced strongly. At the inlet, we enforce $\mathbf{u}$ and $T = T_0$. The axial profile of the radial velocity at the inlet is quadratic and such that the injected mass flow is matched. The axial profile of the azimuthal velocity at the inlet is flat and such that the peak azimuthal velocity approximately matches the tangential velocity in the actual system. Denoting by R_{cap} the radius of the endcap and by H_{in} the height of the axisymmetric inlet, the velocity profiles at the inlet are given

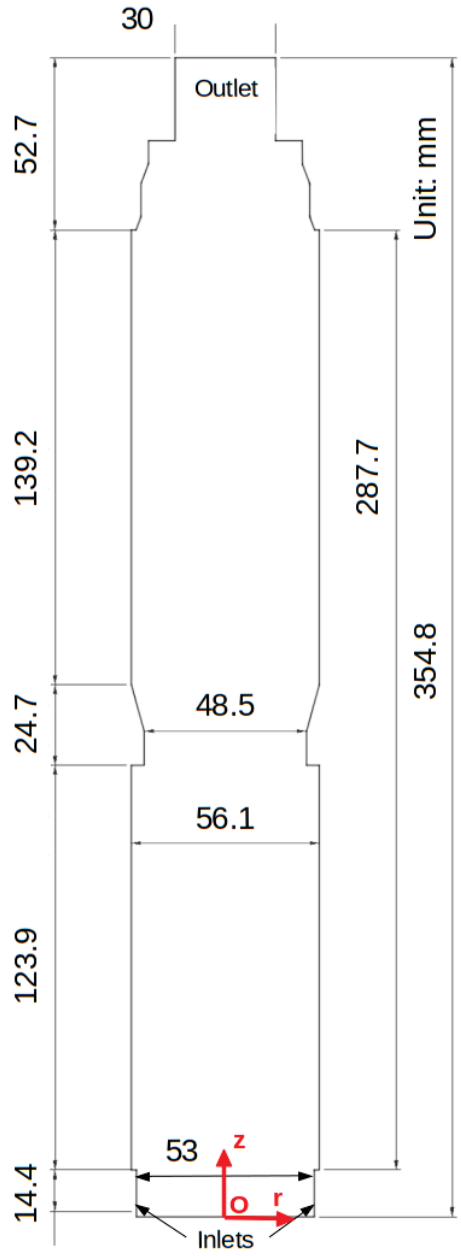

Fig. 4 Schematic of the experimental torch and coordinate reference

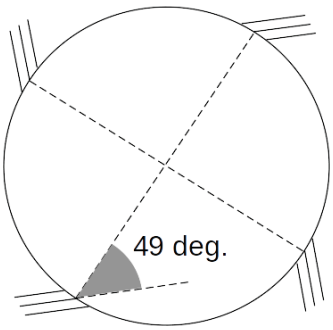

Fig. 5 Top view of the inlet channels and exit angle

by

$$u_r(R_{cap}, z) = -\left(1 - \left(\frac{2z}{H_{in}} - 1\right)^2\right) u_r^0, \ \forall z \in (0, H_{in}), \tag{27}$$

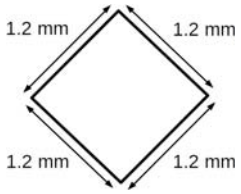

Fig. 6 Inlet channel cross-section

$$u_\theta(R_{cap}, z) = u_\theta^0, \ \forall z \in (0, H_{in}), \tag{28}$$

and

$$u_z(R_{cap}, z) = 0, \ \forall z \in (0, H), \tag{29}$$

where

$$u_r^0 = \frac{3Q_v}{4\pi H_{in} R_{cap}} \tag{30}$$

and

$$u_\theta^0 = \frac{Q_v}{4a^2} \sin\left(\frac{\alpha\pi}{180}\right), \tag{31}$$

with Q_v the injected volume flow, a the inlet side and α the exit angle. The injected volume flow is given by

$$Q_v = \frac{Q_m}{\rho_0}, \tag{32}$$

where $Q_m = 40\rho_{std}/(60 \times 1000)$ is the injected mass flow in kg·s^{-1}, with ρ_{std} the standard air density, and $\rho_0 = p_0/(RT_0)$ is the ambient air density. At the outlet, we enforce $p = p_0$. We use a strong inlet enforcement and a weak outlet enforcement because this combination produces the most stable solution.

The fluid is initially at rest: $\rho = \rho_0$, $\mathbf{u} = \mathbf{0}$ except at the inlet where $\mathbf{u}$ is given by (27)-(29) and $T = T_0$ at $t = 0$. We simulate the system over a time range which allows to observe a regime where the time-averaged fields are almost constant. The time limit is $t_f = 4.3$ s. This time corresponds to approximately 3 flow throughs, one flow through being the time necessary for a fluid particle injected at the inlet to reach the outlet. Note that at this flow rate and geometry, one flow through is approximately 1.3 s.

We present in Table II the parameters considered in this study. The gravity effect is taken into account in this study. There is a factor 2 on the air viscosity used for stability purpose (but which should be reduced to 1 in the future). The mesh is triangular with h varying between 0.06 mm, where the velocity magnitude is the highest (the region close to the inlet), and 1.5 mm. The mesh contains 32313 nodes. The order of approximation is $p = 1$. The time integration is performed by using a 3^{rd} order Runge-Kutta method with a time step $\tau = 1.25 \times 10^{-7}$ s. The azimuthal flow generates an inflow at the outlet. To avoid the crash of the simulation due to this effect, we artificially increase the viscosity close to the outlet by a factor of ≈ 50.

We present in Fig. 7 the time evolution of the kinetic energy. The kinetic energy reaches a pseudo-plateau between 1 and 1.5 s, where it only slightly varies around an average value. This time approximately corresponds to a flow through.

We present in Fig. 8 the components of the velocity at final time. The azimuthal component of the velocity is the strongest component. While decaying in amplitude, it propagates from

TABLE II
TORCH SIMULATION PARAMETERS

Parameter	Value	Unit
R_{cap}	0.0265	m
H_{in}	1.7×10^{-3}	m
a	1.2×10^{-3}	m
α	49	degrees
p_0	1.01325×10^5	Pa
T_0	298.15	K
ρ_{std}	1.184	$\mathrm{kg \cdot m^{-3}}$
g	9.81	$\mathrm{m \cdot s^{-2}}$
R	287	$\mathrm{J \cdot kg^{-1} \cdot K^{-1}}$
γ	1.4	-
η_{ref}	3.69×10^{-5}	$\mathrm{Pa \cdot s}$
T_{ref}	300	K
n_{pl}	0.76	-
Pr	0.707	-

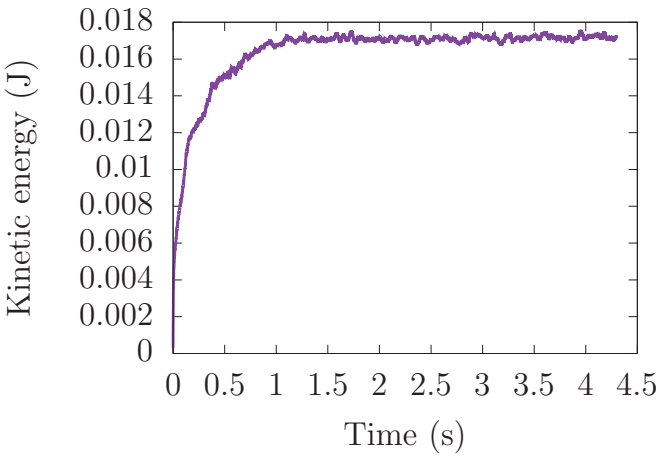

Fig. 7 Torch simulation. Kinetic energy as a function of time

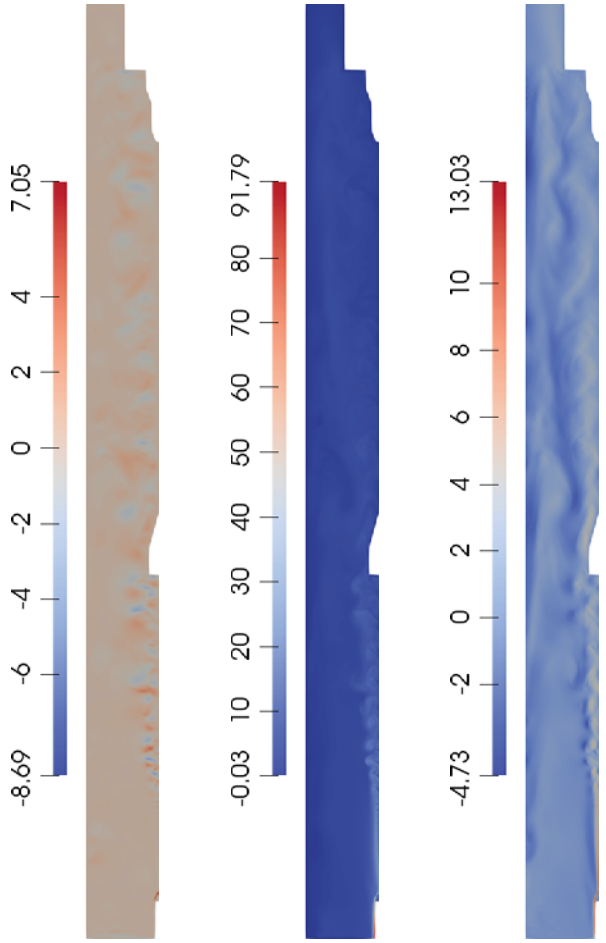

(a) Radial, u_r (b) Azimuthal, u_θ (c) Axial, u_z

Fig. 8 Velocity components in the pseudo-permanent regime (unit: m/s, $t = 4.3$ s)

the inlet to the top of the torch. The flow is essentially concentrated close to the wall in the bottom part of the torch, with a central region with velocities of lower magnitude. Above the narrower section at mid-height, downstream, the velocity field is more uniform in the whole tube.

These observations are confirmed by the profiles of the time-averaged velocity components presented in Fig. 9. The time-averaging is performed from $t = 4$ s to $t = 4.3$ s with a high frequency (10^4 $\mathrm{s^{-1}}$) compared to the time variations of the solution. We present one velocity profile in the bottom compartment (at $z = 0.075$ m) and one in the top compartment (at $z = 0.23$ m). The azimuthal component is the component with the strongest maximum magnitude in both compartments. While the highest velocities are concentrated close to the wall in the bottom compartment, the velocity profiles are more uniform in the top compartment. Note that the flow is not purely upward since the time-averaged axial velocity presents areas of negative values, especially in the top compartment. The flow is structured in layers, with vertical regions of upward flow alternating with regions of downward flow.

In terms of characteristic numbers, the Mach number reaches approximately 0.26 where the velocity magnitude is the strongest, i.e. in the region close to the inlet. Based on the initial density, the velocity at the inlet, the air properties and the torch diameter, the Reynolds number (taking into account sound speed) is of order $10^5 - 10^6$.

VIII. CONCLUSION

We have presented a finite element method to approximate the compressible Navier-Stokes equations, under axisymmetry assumption but taking into account the azimuthal velocity, in order to simulate the flow in a plasma torch geometry. The components of the solution (density, momentum components and energy) are approximated in spaces of continuous axisymmetric functions. The problem is approximated in time with explicit methods. The solving algorithm is implemented in a C++ code, which is first verified with a convergence test against a manufactured solution. The error follows the expected rate when the mesh size is reduced. The code is shown to be able to simulate two classical axisymmetric flows: the Poiseuille flow in a tube and the Taylor-Couette flow, which completes the verification. The final test on an actual

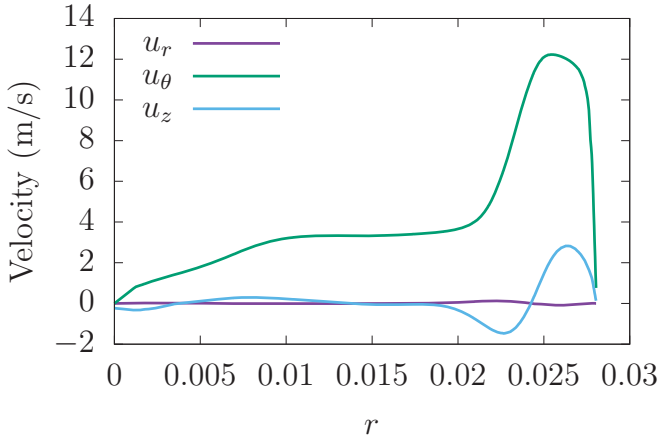

(a) $z = 0.075$ m

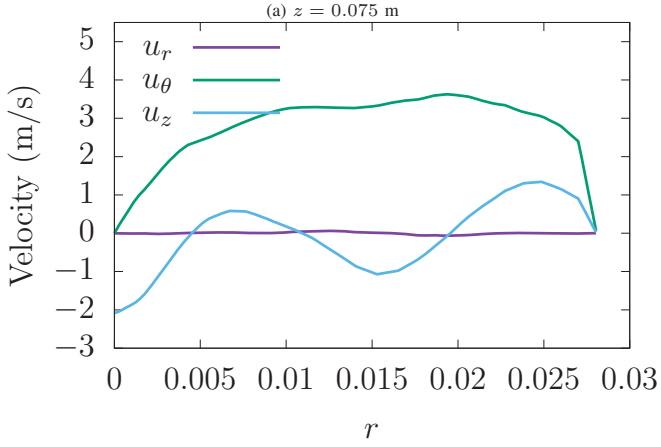

(b) $z = 0.23$ m

Fig. 9 Radial profiles of the time-averaged velocity components ($t = 4.3$ s)

experimental torch setup confirms the interest of our method due to the plausible velocity fields obtained. The velocity fields show a strong swirling flow, subsonic and high-Reynolds, structured in vertical layers of upward and downward flow.

Further torch simulations should be performed with the actual viscosity of air (a factor 2 is used in the article). This task may require updating the numerical method to increase its stability (e.g. implementing the streamline–upwind Petrov/Galerkin method). Comparisons with experiments as well as simulating the jet, and therefore avoiding the artificial viscosity close to the outlet, are also part of future work.

Acknowledgment

This material is based upon work supported by the Department of Energy, National Nuclear Security Administration under Award Number DE-NA0003969.

References

[1] J. Mostaghimi and M. I. Boulos, *Two-Dimensional Electromagnetic Field Effects in Induction Plasma Modelling*, Plasma Chemistry and Plasma Processing 9(1), pp. 25-44, 1989.

[2] S. Clain, D. Rochette, R. Touzani, M. Lino da Silva, D. Vacher and P. André, *A numerical simulation of axisymmetric ICP torches*, Fifth European Conference on Computational Fluid Dynamics, 2010.

[3] B. R. Greene, N. T. Clemens, P. L. Varghese, S. A. Bouslog and S. V. Del Papa, *Characterization of a 50kW Inductively Coupled Plasma Torch for Testing of Ablative Thermal Protection Materials*, 55th AIAA Aerospace Sciences Meeting, 0394, 2017.

[4] S. Clain, D. Rochette and R. Touzani, *A multislope MUSCL method on unstructured meshes applied to compressible Euler equations for axisymmetric swirling flows*, Journal of Computational Physics 13, pp. 4884-4906, 2010.

[5] V. A. Dobrev, T. E. Ellis, T. V. Kolev and R. N. Rieben, *High-order curvilinear finite elements for axisymmetric Lagrangian hydrodynamics*, Computers & Fluids 83, pp. 58-69, 2013.

[6] MFEM: Modular Finite Element Methods library, https://mfem.org.